

**Data Driven Analytics of Porous Battery Microstructures**

Journal:	<i>Energy & Environmental Science</i>
Manuscript ID	EE-ART-02-2021-000454.R1
Article Type:	Paper
Date Submitted by the Author:	15-Mar-2021
Complete List of Authors:	Deva, Abhas; Purdue University, School of Materials Engineering Krs, Vojtech; Purdue University Robison, Lucas; Purdue University, School of Materials Engineering Adorf, Carl; University of Michigan, Chemical Engineering Benes, Bedrich; Purdue University Glotzer, Sharon; University of Michigan, Chemical Engineering Garcia, Edwin; Purdue University, School of Materials Engineering

Cite this: DOI: 00.0000/xxxxxxxxxx

Data Driven Analytics of Porous Battery Microstructures[†]

Abhas Deva,^a Vojtech Krs,^b Lucas D. Robinson,^a Carl S. Adorf,^c Bedrich Benes,^b Sharon C. Glotzer,^c and R. Edwin García ^{*a}

Received Date

Accepted Date

DOI: 00.0000/xxxxxxxxxx

The microstructural optimization of porous lithium ion battery electrodes has traditionally been driven by experimental trial and error efforts, based on anecdotal understanding and intuition, leading to the development of useful but qualitative rules of thumb to guide the design of porous energy storage technology. In this paper, an advanced data-driven framework is presented wherein the effect of experimentally accessible microstructural parameters such as active particle morphology and spacial arrangement, underlying porosity, cell thickness, *etc.*, on the corresponding macroscopic power and energy density is systematically assessed. For the Li_xC_6 | LMO chemistry, an analysis performed on 53,356 battery architectures reported in the literature revealed that for commercial microstructures based on oblate-shaped particles, lightly textured samples deliver higher power and energy density responses as compared to highly textured samples, which suffer from large polarization losses. In contrast, high aspect ratio prolate-shaped particles deliver the highest energy and power density, particularly in the limit of wire-like morphologies. Polyhedra-based colloidal microstructures demonstrate high area densities, and low tortuosities, but provide no appreciable power and energy density benefit over currently manufactured particle morphologies. The developed framework enables to establish general microstructure design guidelines and propose optimal electrode microstructures based on the intended application, given an anode and cathode chemistry.

Broader context

Increasing concerns towards climate change, rising fossil fuel prices, and rapidly emerging electric vehicle markets has only exacerbated the need for high performance LIBs. While significant progress has been made by the development of high capacity, high power density electrode chemistries in the last few decades, battery manufacturing processes remain unoptimized due to a lack of understanding of the fundamental relationships between the performance and the internal microstructure of LIBs. In this paper, an advanced data driven framework is presented to systematically explore such relationships. Guidelines to design microstructurally optimized lithium ion batteries and keep pace with the growing energy requirements are presented.

1 Introduction

Lithium-ion batteries (LIBs) are a well established technology that has become a critical building block of modern society with an

estimated \$40 billion market share in 2018¹, and applications that range from small portable electronics^{1,2}, medium sized devices like laptops and power tools^{1,2}, to large applications such as electric and hybrid vehicles³. In this context, the development of high energy and power density LIBs has traditionally been driven by the introduction of new chemistries, while microstructural optimization has only recently been recognized as key to removing bottlenecks in tuning performance and reliability⁴⁻¹³.

Microstructurally, LIBs are comprised of two porous electrode layers, the anode and the cathode, separated by an electronically insulating layer, called the separator. Each porous electrode layer is an assembly of particles of electrochemically active material that store lithium, surrounded by a conductive binder, liquid electrolyte, and carbon black mixture that facilitates ionic and electronic transport. Microstructural parameters such as morphology, size distribution, and spacial alignment of active particles directly affect the energy and power density of LIBs¹⁴. Strategies to optimize the microstructure of LIBs involve the engineering of one or more of these microstructural parameters^{4,5,15,16}.

For more than 30 years, porous electrode theory²⁰⁻²² has provided the intellectual basis to understand microstructure-performance relationships in LIBs. Microstructural effects are

^a School of Materials Engineering, Purdue University, West Lafayette, Indiana 47907, USA. E-mail: redwing@purdue.edu; Tel: +1-765-494-0148

^b Department of Computer Graphics Technology and Department of Computer Science, Purdue University, West Lafayette, Indiana 47907.

^c Chemical Engineering, University of Michigan, Ann Arbor, MI 48109.

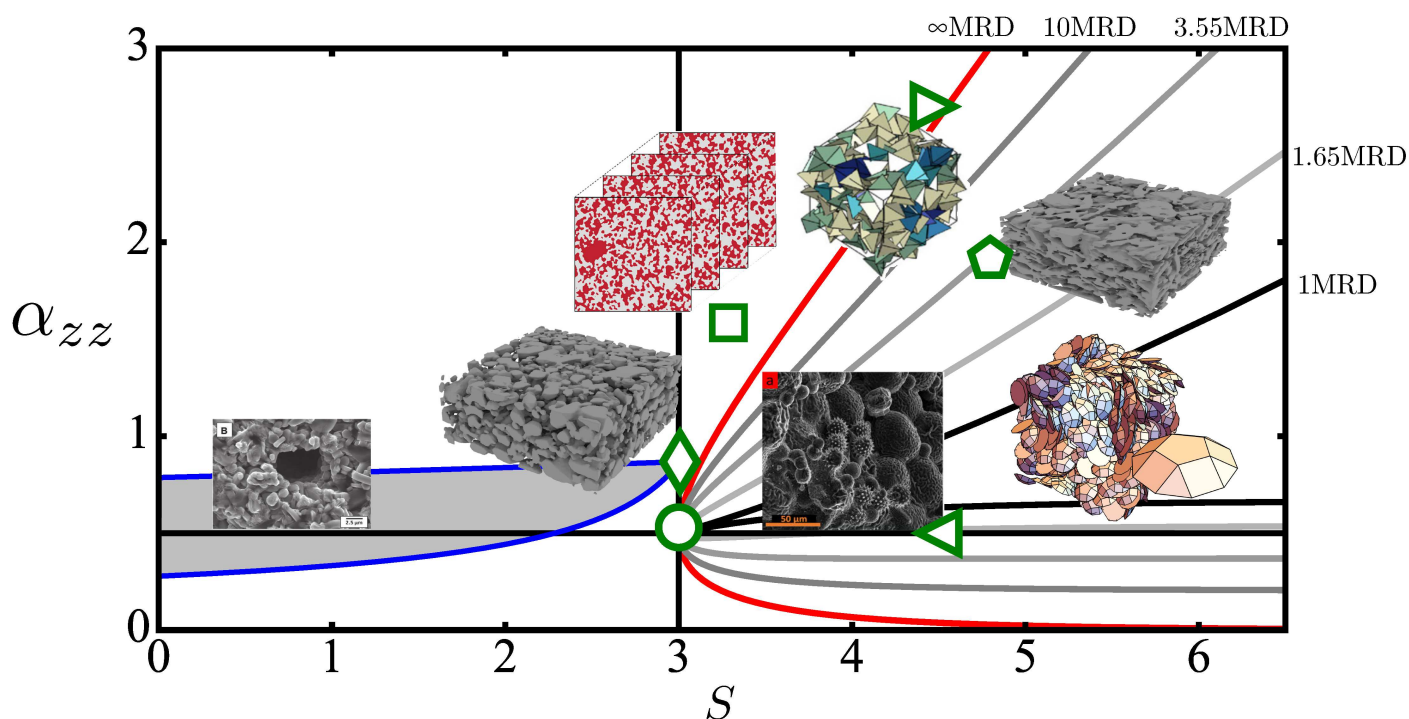


Fig. 1 Normalized area density and Bruggeman exponent for a subset of representative porous electrode microstructures. Example techniques for microstructure engineering include imparting surface roughness⁴, introducing dual porosity⁵, and tailoring the particle morphology^{4,6}. ◁ corresponds to pollen-derived spiky carbon particles, as prepared by Pol and coworkers⁴; ▷ corresponds to jammed systems of tetrahedra, as reported by Smith and Fisher¹⁷; ◻ corresponds to LMO particles, as reported by Gupta, Shyy, and coworkers¹⁸; ◊ corresponds to aligned graphite particles, ◊ corresponds to LCO porous electrodes, and ○ corresponds to perfect spheres and NMC porous electrodes as reported by Ebner, Chung, and coworkers⁶. ◐ corresponds to colloidal nematic microstructures based on pentagonal cupola-shaped particles, as reported by Damasceno, Engel, and Glotzer¹⁹. The gray area bounded by the blue lines corresponds to the tortuosity and area density values accessible by dual porous microstructures as reported by Bae, Chiang, and coworkers⁵. The red curve represents perfectly aligned ellipsoids, the black curve represents randomly oriented ellipsoids while the gray curves represents ellipsoids with intermediate MRD values, 1.65, 3.55, and 10 MRDs. See supplementary information for additional details.

captured through the porosity, reactive area density, and tortuosity of the porous electrodes. Porosity, ε , is defined as the volume fraction of the space left unoccupied by the active particle phase in the electrode. Reactive area density, defined as the electrochemically active surface area per unit volume of the electrode, is typically embodied by relationships of the form^{14,20}:

$$a = \frac{S}{r_p} (1 - \varepsilon) \quad (1)$$

where $r_p = (3V_p/4\pi)^{1/3}$, is the representative length scale associated with the volume of active material particle phase in the electrode, V_p , and S is a geometrical shape factor, defined herein as the normalized reactive area density. $S = 3$ corresponds to spherical particles²⁰, but this value can greatly differ for oblate-shaped particles²³, or particles with a high degree of surface roughness^{15,24,25}.

Similarly, the tortuosity of a porous electrode is a measure of its macroscopic diffusivity or electrical conductivity and has been identified as the key microstructural characteristic that increases polarization losses^{6,26}, particularly at high current densities²⁷.

Here, the Bruggeman relation²⁶:

$$\tau = \frac{1}{\varepsilon^\alpha} \quad (2)$$

has been the engineering touchstone to quantify tortuosity, and minimize transport losses^{14,20}. α is defined as the Bruggeman exponent and captures the statistical contributions of the particle morphology, size distribution, spatial arrangement on the transport of lithium ions around the active particles²⁸. Historically, porous electrodes have been approximated as a monodispersed random distribution of spherical particles by porous electrode theory, *i.e.*, fixing $\alpha = 0.5$ in most of existing applications²⁰⁻²².

Microstructures based on non-spherical particle morphologies include those based on ellipsoids^{6,23}, nanorods^{12,13}, nanowires^{16,29}, nanotubes³⁰, or nanosheets³¹. The morphological anisotropy of such particles translates into anisotropy in the Bruggeman exponent⁶ (α_{xx} , α_{yy} , and α_{zz}) when the microstructure is morphologically textured³². The systematic calculation of the Bruggeman exponent of real microstructures has recently been rationalized by approximating arbitrarily shaped particles by ellipsoids of revolution as a function of the aspect ratio³³, and most recently as a function of morphological texture²³. In this paper, multiples of random distribution (MRD) is introduced as a

measure of the degree of morphological texture, *i.e.*, the degree of particle alignment in a LIB electrode layer. For a microstructure with a morphological texture of n MRDs, the likelihood of finding a particle in a particular orientation is n times greater than the likelihood of finding a particle with the same orientation in a perfectly untextured microstructure. So, in a morphologically textured electrode, $n > 1$, while in an untextured microstructure, $n = 1$. Similarly, a perfectly textured microstructure corresponds to ∞ MRDs. This concept is well established in granular science³⁴, crystallographic texture engineering³⁵, and grain boundary design³⁶. See supplementary information for additional details.

Overall, the microstructural characteristics of a porous electrode are summarized in terms of the normalized area density, S , and the through-thickness Bruggeman exponent, α_{zz} , thus defining a natural space where all the effects of particle morphology, size distribution, and morphological texture can be studied. Figure 1 summarizes a representative portfolio of porous microstructures reported in the scientific literature and highlights the impact of the microstructure on the area density and Bruggeman exponent. The intersection of the lines $S = 3$ and $\alpha_{zz} = 0.5$, corresponds to a porous microstructure of monodispersed random distribution of spherical particles, and divides the space into four distinct quadrants. Here, porous microstructures of oblate particles with different degrees of morphological texture populate the first quadrant while prolate particles populate the fourth quadrant. Away from perfectly spherical particles ($S=3$, $\alpha_{zz} = 0.5$), particle aspect ratio increases along lines of constant MRD. The second and third quadrants can only be accessed by microstructures with a large degree of particle size polydispersity or by using dual porous microstructures⁵. This visualization shows that by using a generalized expression of the through-thickness tortuosity of the Bruggeman relation, existing trends and characteristics in commercial and emerging porous electrodes can be rationalized.

Fundamentally, Figure 1 demonstrates that most of porous battery architectures reported in the literature are caught in a dichotomy: microstructures that are able to increase their reactive area density also increase tortuosity, resulting in power density losses. Microstructures that take advantage of low tortuosity designs, do it at the expense of decreasing their reactive area density. Further, particle alignment induced during electrode calendaring improves the particle packing (and the theoretical energy density as a consequence) but has a negative impact on the through-thickness Bruggeman exponent^{6,14}, thus reducing the delivered power density.

In this paper, the data analytics performed on 53,356 battery electrode layer architectures enable the development of detailed insight into the effect of tortuosity and reactive area density on the corresponding energy and power densities. As an example application, benefits and drawbacks associated with each design are highlighted, given a particle morphology and its spatial distribution, for the well established Li_xC_6 | $\text{Li}_y\text{Mn}_2\text{O}_4$ (LMO) chemistry.

2 Numerical Implementation

The Bruggeman exponent and reaction area density were computed for a total of 53,356 microstructures reported in the liter-

ature^{4,6,17–19,37}. The microstructural data for polyhedra-based colloidal microstructures, was directly made available by Damasceno, Engel, and Glotzer¹⁹ and is comprised of a total of 141 particle morphologies, each having on the order of 10 porosities and 30 samples per porosity. Similarly, publicly available³⁸ graphite, NMC, and LCO microstructures reported by Ebner, Chung, García and Wood⁶ were used as input to predict microstructural battery properties. The Bruggeman exponent and reaction area density were calculated using *Fasτ*³⁹, a GPU-based open-source software framework designed for the high throughput calculation of average microstructural properties of porous electrodes. Each calculation took on the order of 2 mins, for a total ~ 10 days of wall time. Bruggeman exponent values for LFP³⁷, and LMO¹⁸ were used as published, while their normalized reaction area densities were directly estimated from the published images. The Bruggeman exponent of pollen based microstructures⁴ was approximated to that of a monodispersed random distribution of spheres ($\alpha_{zz} = 0.5$) while the normalized reaction area density was calculated from estimates extracted from the published images. The Bruggeman exponent of tetrahedra based microstructures¹⁷ was also readily used as published, while the normalized reaction area density value was ascertained from its surface to volume ratio.

Results show that the through-thickness tortuosity of dual porous microstructures is lowered by high diffusion paths absent of active material particles and the associated reactive area density, as reported by Bae and coworkers⁵. The total porosity $\varepsilon_T = 1 - (1 - \varepsilon_c)(1 - \varepsilon)$ is a function of the porosity of the matrix ε and the volume fraction of the channels, ε_c . The through-thickness tortuosity for a dual porous microstructure is calculated by treating the channels and the matrix as a parallel combination of resistors, $\varepsilon_T/\tau_T = \varepsilon_T^{1+\alpha_T} = \varepsilon_c + (1 - \varepsilon_c)\varepsilon^{1+\alpha_{zz}}$. The average reactive area density of the dual porous microstructure is related to the reactive area density of the matrix through expressions of the form, $S_T = S(1 - \varepsilon_c)^*$.

In order to efficiently capture the effects of microstructure, concentrated solution porous electrode theory was used^{20–22}. This electrochemical analysis was performed for the Li_xC_6 | LMO system in the open source software *dualfoil.py*⁴⁰, which provides a python-based interface that enables the intuitive control of the *dualfoil* legacy code, as made public by Newman and coworkers⁴¹. The software *dualfoil.py* extends the legacy code to consider arbitrary electrode Bruggeman exponents and shape factors as adjustable design parameters, to capture their individual contributions and assess the impact of the electrode microstructure. The effect of the Bruggeman exponent and shape factors of the cathode were analyzed while the values corresponding to the anode were kept fixed. Design adjustable and material parameters are provided in the supplementary information.

To analyze the effect of microstructure on the power and energy density, the normalized reactive area density-Bruggeman exponent space was discretized into intervals of 1 along the area

* For dual porous microstructures, α_T and S_T are used in place of α_{zz} and S in Figures 1 through 4.

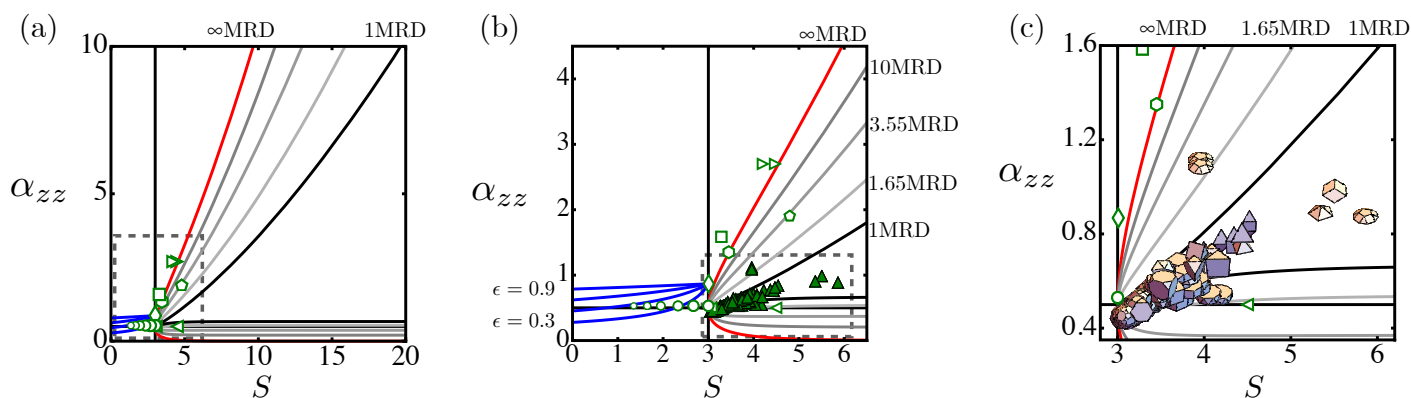





Fig. 2 Reaction area density-Bruggeman exponent space populated by 53,356 microstructures, as reported in the public scientific literature^{4,6,17–19,37}. The red curve represents porous electrodes whose individual particles have an aspect ratio that can be approximated by perfectly aligned ellipsoids of revolution. The black curve represents randomly oriented (morphologically untextured) ellipsoids. Selected shades of gray curves correspond to intermediate values of texture, represented in terms of multiples of random distribution, MRDs: 1.65, 3.55, and 10. \triangleleft corresponds to pollen derived spiky carbon particles prepared by Pol and coworkers⁴; \circ corresponds to values reported by Shearing *et al.* for LFP³⁷; \triangleright corresponds to jammed systems of tetrahedra as reported by Smith and Fisher¹⁷; \square corresponds to LMO particles as reported by Gupta, Shyy, and coworkers¹⁸; \diamond corresponds to aligned graphite particles, \diamond corresponds to LCO porous electrodes and \circ corresponds to NMC porous electrodes as reported by Ebner, Chung, and coworkers⁶. Size of the symbols indicate the degree of polydispersity, ranging from 0.45 to 1. \blacktriangle corresponds to polyhedra-based colloidal microstructures as reported by Damasceno, Engel, and Glotzer¹⁹. Inset (a) shows the complete analyzed space, while inset (b) shows the zoomed-in view (dashed box area in (a)) that corresponds to literature-reported commercial microstructures. Inset (c) shows the zoomed-in view of the region populated by polyhedra-based colloidal microstructures, as highlighted in the dashed box area in (b). Here, markers have been changed to highlight the morphology of the polyhedral active particle¹⁹. The analysis demonstrates that different processing operations, particle morphologies, and ordering of the particles cluster on very specific regions, thus impacting the delivered power and energy density of the cells (see Figures 3 through 5).

density axis and intervals of 0.1 along the Bruggeman exponent axis. The discretization was refined in regions of interest. The relative volume fractions of the constituents in the electrode porosity was held constant for each microstructure without violating maximal random packing limits⁴². Discharge current densities ranging from 1.75A/m² to 122.5A/m² were simulated, resulting in a total of 15,600 simulations representing the space of microstructural parameters, as spanned by the 53,356 battery architectures. On the order of 1,500 simulations did not converge and were discarded without any loss in the resolution of the simulated results.

3 Results and Discussion

Figure 2 shows the reactive area density-Bruggeman exponent space populated by 53,356 porous microstructures reported in the literature^{4,6,17–19,37}. Analytical results based on the differential effective medium approximation, which approximates particles as ellipsoids^{6,23}, are also shown as a means to rationalize the performed numerical simulations. Commercially accessible porous electrodes populate only a subsection of the first quadrant of the space as shown in Figure 2 (b). The large through-thickness Bruggeman exponents and reactive area densities are a consequence of the natural oblate morphology of the active particles as well as the commercially prevalent processing conditions, in agreement with Ebner, Chung, and coworkers⁶. Electrode calendaring induces a high degree of particle alignment resulting in textures higher than 3MRDs. Polyhedra-based colloidal microstructures populate a region between the oblate and prolate branches of the 1MRD (no texture) curve (in black) because of their small aspect ratios and highly organized spacial arrangements¹⁹. This ordering of the particles imposes an upper bound

to the tortuosity of the electrode layers, but enhances the area density by a factor of two with respect to perfectly spherical particles, specifically for colloidal nematic microstructures based on pentagonal cupola-shaped particles , colloidal nematic microstructures based on pentagonal pyramid-shaped particles , and colloidal nematic microstructures based on obtuse golden rhombohedron-shaped particles  (see Figure 2 (c)), demonstrating the possibility of engineering the reactive microstructure without being limited by the polarization losses.

The effects of introducing dual porosity on the reactive area density and through-thickness Bruggeman exponent for an LCO-based porous electrode microstructure is shown in Figure 2 (b). For fixed matrix porosity, ϵ , the through-thickness Bruggeman exponent decreases with the volume fraction of the channels, ϵ_c , at the expense of reactive area and amount of active material. For a fixed ϵ_c value, the lower the matrix porosity, the higher the drop in the through-thickness Bruggeman exponent and the reactive area density. The largest span of the Bruggeman exponent area density space is obtained for microstructures with a high reactive area density and matrix Bruggeman exponent (such as graphite) demonstrating great flexibility in the possibilities of advanced designs. Calculations show that dual porous architectures do not significantly benefit microstructures with small normalized area density and matrix Bruggeman exponent such as NMC (see supplementary information for details).

The effects of microstructure on the energy density of Li_xC₆ | LMO cell is assessed for a current density of 17.5A/m² for the entirety of the analyzed space in Figure 3. Results show that the energy density asymptotically plateaus to a maximum in the region

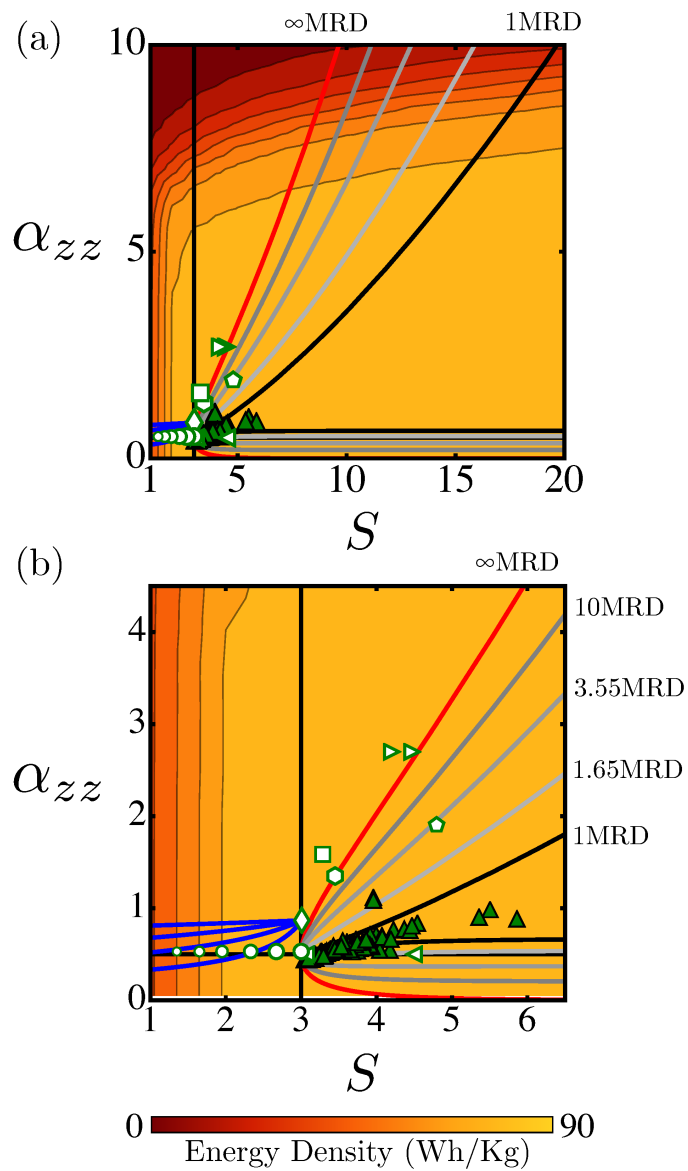


Fig. 3 Energy density response isocontours in normalized reactive area density-Bruggeman exponent space for Li_xC_6 | LMO porous cell for a current density of 17.5A/m^2 . Calculations demonstrate that a space of optimal particle morphologies exist that maximizes the delivered energy density. As commercially accessible electrode designs based on oblate-shaped particles become progressively flatter, the energy density decreases with increasing rate, ultimately passing through a point of inflection. For electrode designs that integrate prolate particles, the energy density increases asymptotically. Inset (a) shows big picture, while inset (b) highlights the subregion of the optimal space accessible by oblate particle morphologies, including commercially accessible microstructures, prolate particle morphologies, as well as polyhedra-based colloidal microstructures.

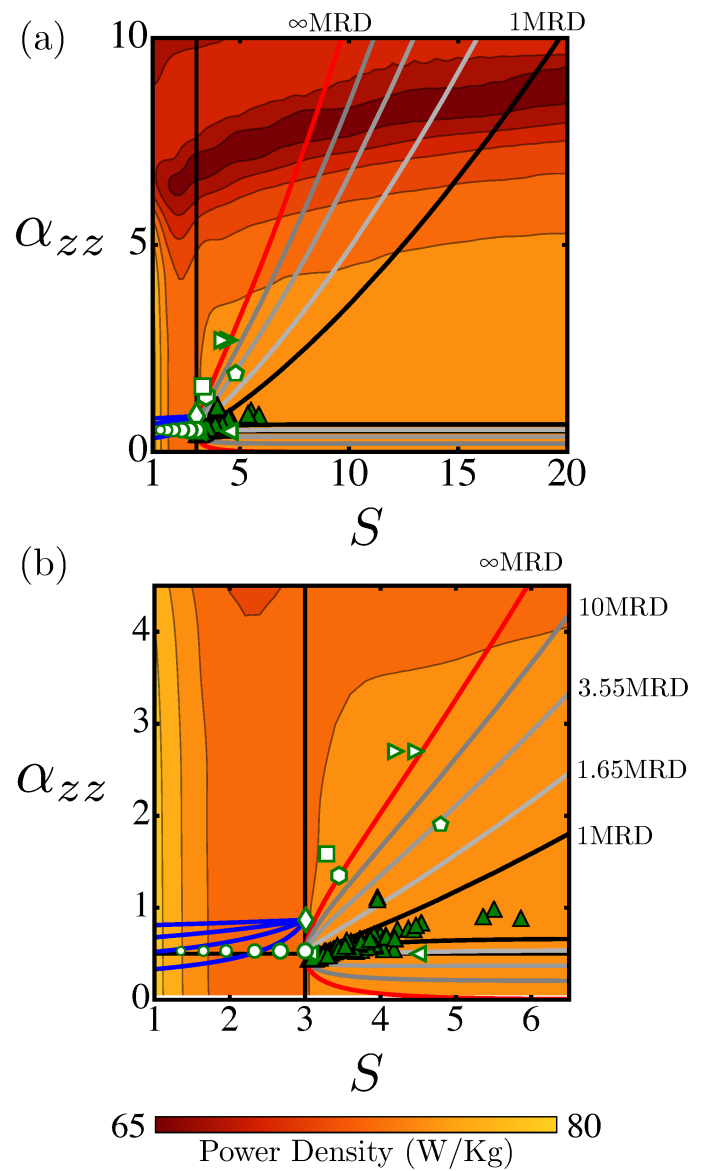


Fig. 4 Power density response isocontours in normalized reactive area density-Bruggeman exponent space for Li_xC_6 | LMO porous cell for a current density of 17.5A/m^2 . Calculations demonstrate that a space of optimal particle morphologies exist that maximizes the delivered power density. As commercially accessible electrode designs conformed of oblate-shaped particles become progressively flatter, the power density asymptotically decreases. For electrode designs that integrate prolate particles, the effect tapers off to advantageous values at high aspect ratios. Inset (a) shows the complete analyzed space, while inset (b) highlights the subregion of the optimal space accessible by oblate particle morphologies, including commercially accessible microstructures, prolate particle morphologies, as well as polyhedra-based colloidal microstructures.

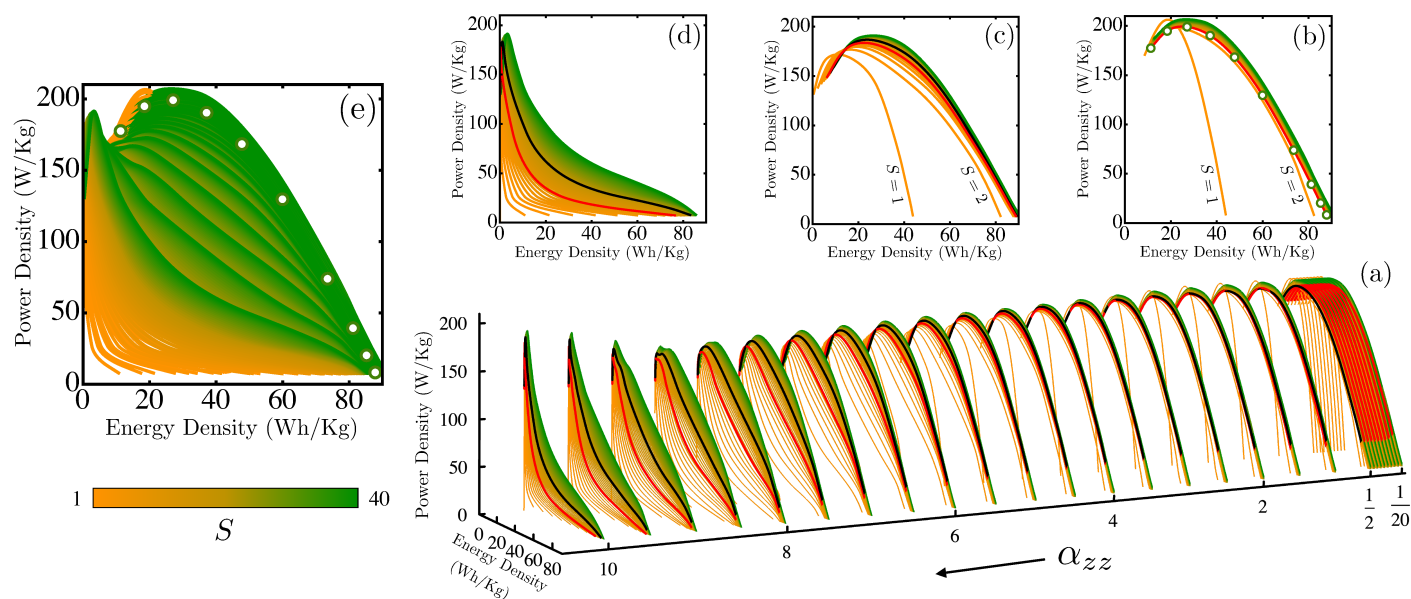


Fig. 5 Effect of microstructural parameters on the Ragone space as spanned by 15,600 porous electrode theory calculations, for a Li_xC_6 | LMO porous cell. Current densities range from $1.75\text{A}/\text{m}^2$ to $122.5\text{A}/\text{m}^2$. Inset (a) shows the Ragone curves as a function of normalized reactive area density and Bruggeman exponent. The red curves highlight microstructures of perfectly aligned ellipsoids (∞ -MRDs) while black curves highlight microstructures with 1MRD. For S values ranging from 1 to 40, inset (b) shows the Ragone curves as a function of shape factor for $\alpha_{zz} = 0.5$, inset (c) shows the Ragone curves as a function of shape factor for $\alpha_{zz} = 5$, and inset (d) shows the Ragone curves as a function of shape factor for $\alpha_{zz} = 10$. Inset (e) shows the entire space of Ragone curves accessible by the analyzed porous electrode microstructures. \circ corresponds to the response delivered by a monodispersed random distribution of spheres. Results show that multiple microstructures deliver identical electrochemical responses. The overlapping highest energy density and the highest power density responses are accessible by commercial microstructures, prolate particle morphologies, as well as polyhedra-based colloidal microstructures (see Figures 3 and 4). Material parameters can be found in the supplementary information.

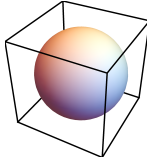
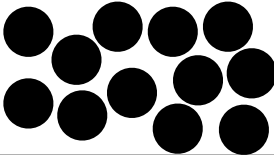
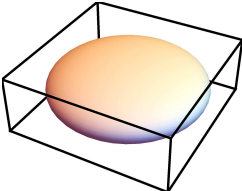
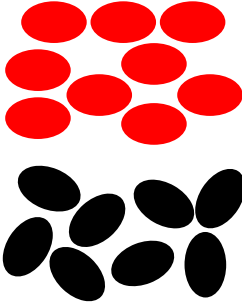
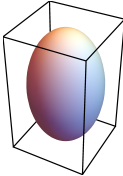
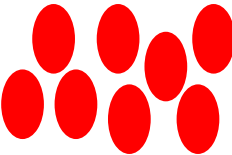
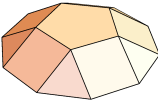
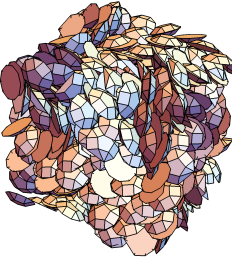
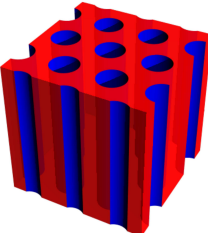
$S \geq 2$ and $\alpha_{zz} \leq 5$. This increase in energy density is attributed to low ohmic losses at low tortuosities along with higher rates of intercalation at large reactive area densities. For currently commercially accessible battery architectures, results demonstrate that an array of optimum average particle morphologies and aspect ratios exist that maximize the energy density output for a fixed degree of texture. Further, the lower the degree of morphological texture, the higher the energy density maximum. Polyhedral and prolate-shaped particles also asymptotically reach the energy density maximum at high aspect ratios as they offer a large reactive area density without a significant increase in the through-thickness Bruggeman exponent.

Figure 4 (a) shows the effect of microstructure on the power density response for the same fixed current density of $17.5\text{A}/\text{m}^2$. For a fixed reactive area density, the power density decreases with increasing through-thickness Bruggeman exponent due to the increase of ohmically-induced through-thickness overpotential. For a fixed Bruggeman exponent, the power density increases with increasing reactive area density due to increased particle electrolyte contact resulting in a higher rate of intercalation. For fixed particle aspect ratio, the power density response of commercially relevant oblate-shaped porous microstructures shows lower power density losses at higher degrees of texture, thus highlighting an unexplored region for microstructure design. For microstructures based on prolate particles, the power density first decreases with increasing aspect ratio due to increased ohmic losses, and then reaches an asymptote for wire-like particles.

Figure 5 (a) summarizes the effect of microstructure on the Ragone plot response. Each curve corresponds to an (S, α_{zz}) pair in Figure 2 (a). For a fixed (S, α_{zz}) pair, as the current density increases, the power density increases at the expense of the energy density due to increased polarization losses. For the analyzed chemistry, the delivered power density goes through a maximum for a current density of $\sim 87.5\text{A}/\text{m}^2$. Larger current densities increase the polarization losses which inhibit the power density. Overall, results show that a Bruggeman exponent $\alpha_{zz} \approx 0.05$, and an area density $S \approx 40$ delivers an energy density that is the closest to the theoretical ideal. This corresponds to a microstructure of aligned wire-like shaped particles (limiting case of very large aspect ratio prolate particles) with a morphological texture > 10 MRD. This demonstrates the power of data analytics, enabling the identification of battery architectures, far away from what has been previously sought.

Figure 5 (b) and (c) shows that all the colloidal-type and prolate-shape particle designs ($S \geq 2, \alpha_{zz} < 3$) deliver power and energy density responses that are virtually indistinguishable, but relevant: As α_{zz} increases, the maximum delivered power density asymptotically decreases. The effect of the rest of the individual microstructural parameters become apparent for Bruggeman exponents $\alpha_{zz} > 4$, which are accessible by oblate-shaped particles, see Figure 5 (c). The effect of alignment favors larger area density values which dominates the power density response (Figure 5 (e)). Here, large Bruggeman exponents contribute to high power densities for large area densities, as a result of the ohmic

Table 1 Summary of effect of microstructure on the performance of a Li_xC_6 | LMO porous cell. Through-thickness direction corresponds to the vertical z-direction.

morphology	microstructure	highlights
sphere 		Delivers low tortuosities and reactive area densities. Suitable for high power density applications due to low through-thickness polarization losses. This particle morphology and the associated microstructure is widely assumed, but remains a poor approximation of porous LIB electrodes.
oblate 		Found in most of commercially available microstructures. Suffer large through-thickness polarization losses due to particle alignments induced during electrode calendaring, thus lowering both energy and power densities. Small aspect ratios can increase the power density without inducing large (tortuosity-dominated) polarization losses. Power and energy densities can be increased by inducing mild textures (particle alignments), while tailoring the corresponding area density.
prolate 		Delivers the overall highest energy and power density responses of the analyzed microstructures, particularly in the limit of wire-like morphologies and alignments toward the counter electrode.
polyhedron 		Delivers tortuosities and reactive area densities between those displayed by untextured oblate-shaped and prolate-shaped particles but offer no significant advantage in-terms of power and energy densities over currently used commercial microstructures.
dual porous 		Effective way to tailor the total tortuosity and reactive area density for microstructures with high matrix tortuosities and reactive area densities to specific power and/or energy density applications.

losses-induced overpotential, which favor the local intercalation kinetics. However, degradation mechanisms will also be favored under these conditions⁴³.

It is important to note that the power and energy density response is also a function of other microstructural design parameters such as particle size, electrode porosity, cell thickness, initial lithium concentration, *etc.* For example, results show that decreasing the thickness of the anode and cathode layer of the cell while keeping the theoretical capacity ratio fixed decreases diffusion distances thereby resulting in a higher power density response. In contrast, increasing the thickness of the anode and cathode layers while keeping the theoretical capacity ratio fixed increases diffusion distances thereby resulting in lower power densities even as the energy density increases (see supplementary information for details). Cells based on spherical particles and polyhedra-based colloidal microstructures benefit from using thinner electrode layers for high power density applications, while thicker electrochemical cells based on high aspect ratio particle morphologies are more favourable in high energy density applications.

Also, increasing the cathode porosity increases the lithium transport rate while decreasing underutilized mass of the cathode. Results show that both the energy and power densities increase. However, microstructures based on spherical particles display a marked drop in the power density response as the cathode porosity is increased. This is because at higher porosities, lithium transport becomes faster even though the total electrochemically active area decreases. Therefore, battery architectures based on high aspect ratio morphologies, both prolate and oblate, benefit from increased porosity (see supplementary information for details).

4 Summary and Conclusions

A data driven approach was developed to analyze the impact of a wide range of microstructural parameters on the power and energy density response of LIBs using the well established Li_xC_6 | LMO cell as an example application. The most relevant and important microstructural effects are summarized in Table 1. Specifically for microstructures based on oblate-shaped particles of active material, microstructural alignment induced during electrode compaction and calendaring results in large tortuosity-induced through-thickness polarization losses, and thus low energy and power densities. In contrast, lightly textured microstructures based on oblate-shaped particles improve both the energy and power density responses. Prolate-shaped particles offer large reactive area densities without a significant increase in the through-thickness Bruggeman exponents, thus deliver an overall maximum on the energy and power density response at high particle aspect ratios, in the limit of wire-like morphologies. Polyhedra-shaped particles deliver microstructural properties between those displayed by untextured oblate and prolate-shaped particles because of their small aspect ratios and highly organized spacial arrangements. However, polyhedra-shaped particles do not offer any significant improvement in the energy and power density response as compared to currently prevalent commercial microstructures. Dual porous designs are an efficient method to tune

the microstructural characteristics of porous electrodes and are especially beneficial for microstructures with large normalized area densities and matrix Bruggeman exponents such as those displayed by graphite.

Overall, the developed infrastructure presented herein lays down the foundation to accelerate the analysis of the microstructural parameters and their impact on the Ragone plot response of new and advanced battery designs and rapidly identify advantageous chemistries and architectures, as well as the associated processing operations that will inexpensively maximize the performance and minimize the degradation of LIBs in the decades to come.

5 Conflicts of Interest

There are no conflicts of interest to declare.

6 Acknowledgments

AD and REG thank the support provided by TRI. VK, REG, and BB thanks the support of NSF grant #1608762, *Inverse Procedural Material Modeling for Battery Design*. CSA and SCG acknowledge the National Science Foundation, Division of Materials Research Award # DMR 1409620 and the computational resources and services supported by Advanced Research Computing at the University of Michigan, Ann Arbor.

Notes and references

- 1 C. Pillot, 36th Annual International Battery Seminar & Exhibit. Avicenne Energy, 2019.
- 2 G. Zubi, R. Dufo-López, M. Carvalho and G. Pasaoglu, *Renewable and Sustainable Energy Reviews*, 2018, **89**, 292–308.
- 3 X. Zeng, M. Li, D. Abd El-Hady, W. Alshitari, A. S. Al-Bogami, J. Lu and K. Amine, *Advanced Energy Materials*, 2019, **9**, 1900161.
- 4 J. Tang, V. Etacheri and V. G. Pol, *Scientific Reports*, 2016, **6**, 20290.
- 5 C. J. Bae, C. K. Erdonmez, J. W. Halloran and Y. M. Chiang, *Advanced Materials*, 2013, **25**, 1254–1258.
- 6 M. Ebner, D. W. Chung, R. E. García and V. Wood, *Advanced Energy Materials*, 2014, **4**, 1–6.
- 7 C. Jiang, M. Wei, Z. Qi, T. Kudo, I. Honma and H. Zhou, *Journal of Power Sources*, 2007, **166**, 239–243.
- 8 A. S. Arico, P. Bruce, B. Scrosati, J.-M. Tarascon and W. Van Schalkwijk, *Nature materials*, 2005, **4**, 366–377.
- 9 J. Chen and F. Cheng, *Accounts of chemical research*, 2009, **42**, 713–723.
- 10 Y.-G. Guo, J.-S. Hu and L.-J. Wan, *Advanced Materials*, 2008, **20**, 2878–2887.
- 11 H. Li, Z. Wang, L. Chen and X. Huang, *Advanced Materials*, 2009, **21**, 4593–4607.
- 12 L. Peng, H. Zhang, Y. Bai, J. Yang and Y. Wang, *Journal of Materials Chemistry A*, 2015, **3**, 22094–22101.
- 13 J. Liu, C. Liu, Y. Wan, W. Liu, Z. Ma, S. Ji, J. Wang, Y. Zhou, P. Hodgson and Y. Li, *CrystEngComm*, 2013, **15**, 1578–1585.
- 14 D. W. Chung, M. Ebner, D. R. Ely, V. Wood and R. E. García,

- Modelling and Simulation in Materials Science and Engineering*, 2013, **21**, 74009–74025.
- 15 W. Li, F. Wang, Y. Liu, J. Wang, J. Yang, L. Zhang, A. A. Elzatahry, D. Al-Dahyan, Y. Xia and D. Zhao, *Nano letters*, 2015, **15**, 2186–2193.
- 16 J. Wang, Q. Zhang, X. Li, D. Xu, Z. Wang, H. Guo and K. Zhang, *Nano Energy*, 2014, **6**, 19–26.
- 17 K. C. Smith and T. S. Fisher, *Journal of Heat Transfer*, 2013, **135**, 081301.
- 18 A. Gupta, J. H. Seo, X. Zhang, W. Du, A. M. Sastry and W. Shyy, *Journal of The Electrochemical Society*, 2011, **158**, A487.
- 19 P. F. Damasceno, M. Engel and S. C. Glotzer, *Science*, 2012, **337**, 453–457.
- 20 T. F. Fuller, M. Doyle and J. Newman, *Journal of the Electrochemical Society*, 1994, **141**, 1–10.
- 21 C. M. Doyle, *PhD thesis*, University of California, Berkeley, CA, 1995.
- 22 M. Doyle, J. Newman, A. S. Gozdz, C. N. Schmutz and J.-M. Tarascon, *Journal of the Electrochemical Society*, 1996, **143**, 1890–1903.
- 23 R. García-García and R. E. García, *Journal of Power Sources*, 2016, **309**, 11–19.
- 24 R. Paul, V. Etacheri, V. G. Pol, J. Hu and T. S. Fisher, *RSC Advances*, 2016, **6**, 79734–79744.
- 25 R. A. Adams, A. D. Dysart, R. Esparza, S. Acuña, S. R. Joshi, A. Cox, D. Mulqueen and V. G. Pol, *Industrial & Engineering Chemistry Research*, 2016, **55**, 8706–8712.
- 26 D. A. G. Bruggeman, *Annalen der Physik*, 1935, **416**, 636–664.
- 27 F. Pouraghajan, H. Knight, M. Wray, B. Mazzeo, R. Subbaraman, J. Christensen and D. Wheeler, *Journal of The Electrochemical Society*, 2018, **165**, A2644–A2653.
- 28 I. V. Thorat, D. E. Stephenson, N. A. Zacharias, K. Zaghbi, J. N. Harb and D. R. Wheeler, *Journal of Power Sources*, 2009, **188**, 592–600.
- 29 Y. Li, B. Tan and Y. Wu, *Nano letters*, 2008, **8**, 265–270.
- 30 W.-Y. Li, L.-N. Xu and J. Chen, *Advanced Functional Materials*, 2005, **15**, 851–857.
- 31 S.-H. Yu, D. J. Lee, M. Park, S. G. Kwon, H. S. Lee, A. Jin, K.-S. Lee, J. E. Lee, M. H. Oh, K. Kang *et al.*, *Journal of the American Chemical Society*, 2015, **137**, 11954–11961.
- 32 M. H. Zimmerman, K. Faber, E. R. Fuller Jr, K. L. Kruger and K. J. Bowman, *Journal of the American Ceramic Society*, 1996, **79**, 1389–1393.
- 33 M. Ebner and V. Wood, *Journal of The Electrochemical Society*, 2014, **162**, A3064.
- 34 V. R. Vedula, S. J. Glass, D. M. Saylor, G. S. Rohrer, W. C. Carter, S. A. Langer and E. R. Fuller Jr, *Journal of the American Ceramic Society*, 2001, **84**, 2947–2954.
- 35 J. E. Blendell, M. D. Vaudin and E. R. Fuller, *Journal of the American Ceramic Society*, 1999, **82**, 3217–3220.
- 36 G. S. Rohrer, D. M. Saylor, B. E. Dasher, B. L. Adams, A. D. Rollett and P. Wynblatt, *Zeitschrift für Metallkunde*, 2004, **95**, 197–214.
- 37 S. J. Cooper, D. S. Eastwood, J. Gelb, G. Damblanc, D. J. L. Brett, R. S. Bradley, P. J. Withers, P. D. Lee, A. J. Marquis, N. P. Brandon and P. R. Shearing, *Journal of Power Sources*, 2014, **247**, 1033–1039.
- 38 M. Ebner, D. W. Chung, R. E. García and V. Wood, *Battery Microstructure Project*, Accessed Spring, 2019, <https://made.ee.ethz.ch/research/open-source-data-an>
- 39 V. Krs, A. Deva, R. E. García and B. Benes, *Fast: Accelerated Data Driven Microstructural Design of Porous Electrodes for Battery Applications*, Accessed Spring, 2019, <https://github.com/krsvojte/fast>.
- 40 L. D. Robinson and R. E. García, *Dualfoil.py: Porous Electrochemistry for Rechargeable Batteries*, Accessed Fall, 2017, <https://nanohub.org/resources/dualfoil>.
- 41 J. Newman, *FORTRAN Programs for the Simulations of Electrochemical Systems (dualfoil5.2.f)*, Accessed Spring, 2015, <http://www.cchem.berkeley.edu/jsngrp>.
- 42 A. Donev, I. Cisse, D. Sachs, E. A. Variano, F. H. Stillinger, R. Connelly, S. Torquato and P. M. Chaikin, *Science*, 2004, **303**, 990–993.
- 43 D. Aurbach, E. Zinigrad, Y. Cohen and H. Teller, *Solid state ionics*, 2002, **148**, 405–416.